Computers and Geotechnics 157 (2023) 105275

Contents lists available at ScienceDirect

Computers and Geotechnics

journal homepage: www.elsevier.com/locate/compgeo

Finite element modelling of rolling dynamic compaction

Andrew C. Bradley *, Mark B. Jaksa *, Yien-Lik Kuo

School of Civil, Environmental and Mining Engineering, University of Adelaide, SA 5005, Australia

ARTICLE INFO

Keywords:
Rolling Dynamic Compaction
Impact Roller
Ground Improvement

ABSTRACT

Rolling dynamic compaction (RDC) utilises a heavy (6 to 12-tonne) non–circular module (impact roller) that pivots about its corners as it is towed, causing the module to fall to the ground and compact the underlying soil dynamically. This paper presents the development of a transient, non–linear finite element (FE) model of the Broons BH–1300 4–sided 8 tonne impact roller, undertaking multiple passes, using LS–DYNA, validated against a field trial and observations presented in the literature for the same coarse–grained material. The results of the numerical analyses demonstrate that the FE model provides reliable predictions of the 4-sided roller as observed in the field. Thus, the use of this FE model may provide high resolution insights into the capability of the impact roller, namely in predicting the settlement and densification of an underlying coarse-grained material. The FE model demonstrates significant soil improvement directly beneath the width of the roller to approximately 1.2 m depth. Residual improvement is shown to extend to approximately 2.5 m depth and 1.25 m laterally.

1. Introduction

Rolling dynamic compaction (RDC) is a ground improvement technology that involves the use of a non–cylindrical rolling module incorporating 3, 4 or 5 sides. The module rotates about its corners as it is towed and falls to the ground, compacting it dynamically. Despite several field-based studies, and limited laboratory-based research, the depth to which RDC improves a given soil, for a specified number of passes (N), is not yet fully understood. To date, very limited numerical studies have been undertaken to model RDC, the first of which, was performed by Kim (2010) using the finite element method (FEM) within LS-DYNA (LSTC, 2015). Since then, the FEM, which provides an appropriate methodology for modelling the complexities of non-linear soil mechanics, has also been applied, to a limited extent, to RDC by Bastaee & Parvizi (2012); Bradley et al. (2012), Kuo et al. (2013), and Li (2021). As an alternative to FEM, a discrete element method (DEM) approach was undertaken by Chen et al. (2021). In brief, these studies provide insight into the potential of RDC. With exception of Li (2021) and Chen et al (2021), a single pass of a specific design of roller was typically modelled, and as such, did not consider the normal RDC practice of performing multiple passes, nor were the results validated against controlled field tests.

Further, these prior studies have the common limitation of adopting limited material models to represent the dynamic and large strain soil behaviour evident in RDC. In particular, the Drucker-Prager model within LS-DYNA (i.e. Mat_193) is commonly used. This model accounts for shear yield behaviour, but only models linear-elastic volumetric behaviour. As a result, settlement and densification is likely to be inadequately represented. Given that a key performance indicator for RDC is the densification of the soil, consideration for modelling volumetric behaviour is critical. In contrast, this paper incorporates the geological cap model (GCM) supplied within LS–DYNA (i.e. Mat_025) as it not only models volumetric plastic strains but also accounts for dilation and a collapsible cap yield surface initiated by shearing.

Additionally, each of the numerical studies within the literature have assumed the motion of the module; typically, a constant horizontal velocity and angular velocity about the roller's axle. By assuming the roller's motion, the interaction between the roller and the soil surface, and hence the magnitude of the compactive energy imparted to the underlying soil, is not necessarily representative of the true behaviour. Further, the motion of the 4-sided roller is complicated by the fact that the roller is non–cylindrical, and it incorporates a double linkage spring support mechanism, which stores energy from, and releases it to, the module in order to enhance rolling and improve compactive performance. Understandably, these assumptions were made largely due to the absence of information at the time, regarding the kinematics of, and the energy imparted by, the module.

Since then, Bradley et al. (2019) presented the results of a field trial of the BH–1300, 8 tonne, 4–sided impact roller on a 12 × 7.5 m test bed, excavated to 1.5 m depth. The test bed was backfilled with a local sandy gravel fill material; the same fill material used in field investigations by

* Corresponding authors.
E-mail addresses: Andrew.Bradley@adelaide.edu.au (A.C. Bradley), Mark.Jaksa@adelaide.edu.au (M.B. Jaksa).

https://doi.org/10.1016/j.compgeo.2023.105275
Received 6 October 2022; Received in revised form 26 December 2022; Accepted 15 January 2023
Available online 24 February 2023

Nomenclature

c'	effective cohesion
$\bar{C}$	Mat_025 kinematic hardening parameter
d	Drucker–Prager cohesion
$\measuredangle_0$	initial depth
D	Mat_025 volumetric parameter
DoI	depth of improvement
Dr	relative density
Dr_0	initial relative density
e	void ratio
e_0	initial void ratio
e_L	virgin compression line void ratio intercept
e_{max}	maximum void ratio
e_{min}	minimum void ratio
E	Young's modulus
$E_{absorbed}$	energy absorbed by the soil per impact
E_{lost}	roller energy lost per impact
$E_{kinetic}^{peak}$	peak kinetic energy per impact
FD	coefficient of dynamic friction
FS	coefficient of static friction
G	elastic shear modulus
G_s	specific gravity of the solids
i	number of completed passes
I_1	first invariant of stress tensor
I_r	improvement index
$I_{r\|max}$	max. I_r along *length of interest* w.r.t N, $\measuredangle_0$, LO
$I_{r\|ave}$	average I_r along *length of interest* w.r.t N, $\measuredangle_0$, LO
$I_{r\|min}$	min. I_r along *length of interest* w.r.t N, $\measuredangle_0$, LO
$I_{r\|max}^*$	max. I_r across *length of interest* w.r.t N, $\measuredangle_0$, and $LO \in [0.05, 0.65$ m$]$
$I_{r\|ave}^*$	average I_r across *length of interest* w.r.t N, $\measuredangle_0$, and $LO \in [0.05, 0.65$ m$]$
$I_{r\|min}^*$	min. I_r across *length of interest* w.r.t N, $\measuredangle_0$, and $LO \in [0.05, 0.65$ m$]$
$\widehat{I}_{r\,field}$	improvement index prediction model inferred from field trial
J_{2D}	second invariant of deviator stress
K	elastic bulk modulus
L	added vertical loading to each node of the roller
LO	initial lateral offset from the centreline of the roller's path
M	Drucker-Prager slope
N	number of passes
$\bar{N}$	Mat_025 kinematic hardening parameter
p	mean pressure
p_c	apparent preconsolidation pressure
p_{max}	selected max pressure to calibrate volumetric behaviour
q	deviator stress
r_i	set of reset offsets
R	Mat_025 shear envelope parameter
S	surface settlement
$\widehat{S}_{field}$	settlement prediction model inferred from field trial
T	Mat_025 shear envelope parameter
V_h	roller forward horizontal velocity
V_v	roller vertical velocity
$\widehat{V}_x$	*typical motion* forward horizontal velocity
$\widehat{V}_y$	*typical motion* vertical velocity
W	Mat_025 volumetric parameter
X_0	Mat_025 volumetric parameter
α	Mat_025 shear envelope parameter
β	Mat_025 shear envelope parameter
γ	Mat_025 shear envelope parameter
$\varepsilon_{v\|CC}$	Cam–Clay total volumetric strain
$\varepsilon_{v\|GCM}$	Mat_025 total volumetric strain
$\varepsilon_{v\|GCM}^e$	Mat_025 elastic volumetric strain
$\varepsilon_{v\|GCM}^p$	Mat_025 plastic volumetric strain
θ	Mat_025 shear envelope parameter
κ	logarithmic slope of unload – reload line
λ	logarithmic slope of virgin compression line
μ	coefficient of friction
ν	Poisson's ratio
ρ	Mat_025 mass density
ρ_0	initial bulk density
$\rho_{d\|0}$	initial dry density
σ_V^A	applied vertical stress
σ_V	total vertical stress
σ_{V0}	initial overburden
φ'	effective internal angle of friction
φ'$_{cv}$	critical state effective internal angle of friction
ω_l	roller angular velocity
$\widehat{\omega}_x$	*typical motion* angular velocity
Ω	roller orientation

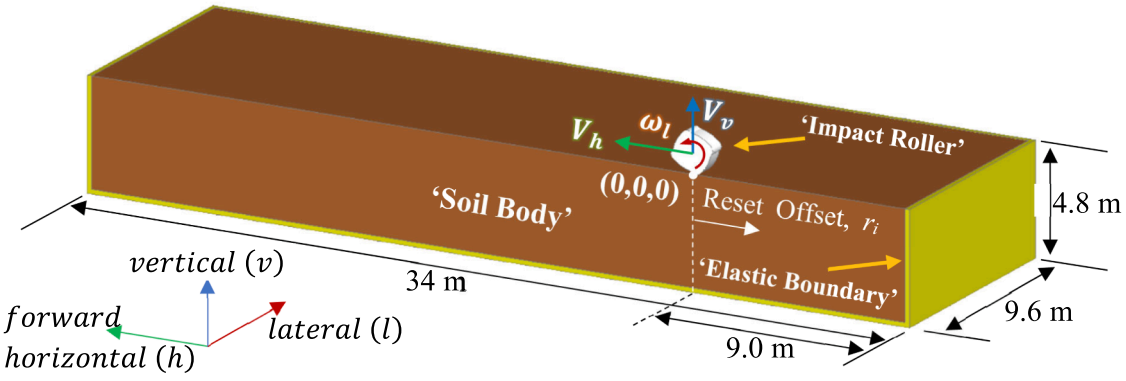

Fig. 1. Global model layout in LS–DYNA.

Table 1
GCM material model inputs.

Mass Density	Elasticity		Failure Envelope						Plastic Volumetric Strain			Kinematic Hardening	
ρ	K	G	α	θ	γ	β	R	T	X_0	D	W	$\bar{C}$	$\bar{N}$
t/mm^3	MPa	MPa	MPa	–	MPa	–	–	MPa	MPa	MPa^{-1}	–	–	–
1.88E-9	44.9	16.1	0.0462	0.302	0	0	3.308	0.003	0	0.503	0.0572	0	0

Canala et al. (2014) and Scott et al. (2016, 2019a).

The kinematics of the roller during the field trial were analysed by Bradley et al. (2019) to produce a representative *typical motion* of the roller's horizontal velocity $(\widehat{V}_x)$, vertical velocity $(\widehat{V}_y)$, and angular velocity about its axle $(\widehat{\omega}_x)$. From this study, the energy of the roller lost, and potentially delivered to the soil, through each impact under *typical motion* was estimated to be 23 ± 4 kJ, and the peak kinematic energy of the roller to be 62 ± 3 kJ; both of which are in general agreement with estimations by Clifford & Bowes (1995) and Scott et al. (2020).

This paper aims to develop a finite element (FE) model which accurately simulates the complex behaviour and interaction between the Broons BH–1300 4-sided 8–tonne impact roller and an underlying coarse-grained soil subject to multiple passes, in order to produce reliable estimates of the surface settlement and the compaction of soil at depth. This is achieved by implementing field–validated motion of the roller by Bradley et al. (2019) and comparing the model predictions of ground settlement and in situ density with field measurements. A field trial, presented herein, provides the basis from which to verify the model. Moreover, as a check on the resolution of the FE mesh, this paper compares and assesses the results of a relatively fine FE mesh to one that is coarser. To assist processing of the model, the University of Adelaide's high-performance computing facility, Phoenix (University of Adelaide, 2020), was necessary.

2. Model Formulation

A three–dimensional formulation is used, as summarised in Fig. 1, with a half–space symmetry along the centreline of the roller's path. The model comprises three parts: the roller, the soil body, and the elastic boundary.

The global model is subject to a vertical global gravity load. Additionally, a nominal 1 kPa overburden load is placed across the soil surface to assist with model initialisation. Dynamic relaxation is invoked to initialise the model with respect to the gravity and overburden loading to converge towards a quasi–static state before proceeding to a transient phase.

Two cases are considered separately: (1) a static case in which the roller is placed on the soil at rest; and (2) a dynamic case in which the roller undertakes multiple passes. The static case of the roller resting on the ground surface is benchmarked against at–rest in situ stresses reported by Scott et al. (2019b). The dynamic case of the impact roller undertaking 30 passes, 10 impacts per pass, is benchmarked against a field study, presented in Section 3, in addition to the findings of Canala et al. (2014), Bradley et al. (2019) and Scott et al. (2016, 2019b).

2.1. Soil body model

The soil body is modelled as a homogenous material. As mentioned previously, the GCM (Mat_025) is adopted as the constitutive model for the soil body; a brief description of its formulation and how the input parameters are determined within this study is presented in Section 2.2.

The dimensions of the soil body are selected such that a sufficient length of soil permits at least 10 impacts per pass, whilst simultaneously providing some additional distance to mitigate potential boundary effects. Furthermore, given the roller is undertaking multiple passes, additional length along the roller's path, ahead and behind, is necessary to account for potential repositioning of the roller for each pass during the resetting phase, as detailed in Section 2.4 below.

A non–reflecting boundary is defined along the outer perimeter of a 200 mm thick elastic boundary that surrounds the soil body; along the sides and underneath, as shown in Fig. 1. Nodes along the interface of the soil body and elastic boundary tie them together. The stiffness of the elastic boundary is assumed to be hard, such that the Young's modulus (E) and Poisson's ratio (ν) for the elastic boundary are $E = 431$ MPa, and $\nu = 0.34$, respectively.

The soil body and boundary are constructed using solid, 8–node hexahedrons (ELFORM = 1). Further, Belytschko & Bindeman's (1993) hourglass control formulation (IHQ = 6) is used. Two resolutions of the FE mesh are considered: (1) a fine FE mesh built from $100 \times 100 \times 100$ mm FEs; and (2) a coarse FE mesh built from $200 \times 200 \times 200$ mm FEs.

Rayleigh viscous damping is considered to represent the internal material damping of the soil. In a similar manner to the FE models by Gu & Lee (2002) and Bradley et al. (2015) for coarse-grained material, and in agreement with the typical values presented by Santamarina & Park (2016), a damping ratio of 5% of critical, for lower and upper reference frequencies of 0.01 Hz and 100 Hz, is considered.

2.2. Geological cap model

To account for densification, and thereby improvement, of the soil subject to RDC, an inelastic constitutive material model with capability to articulate both volumetric and shear behaviour is required. The GCM (Mat_025) is selected as the constitutive model for the soil body.

The GCM is an extended two invariant cap model, with an associated flow rule, based on the formulations by Isenberg et al. (1978), Sandler & Rubin (1979), and Simo et al. (1988). In brief, GCM has capabilities in modelling shear behaviour, in addition to elastic–plastic volumetric behaviour and rate dependent kinematic hardening. However, the kinematic hardening feature will not be considered within the scope of this study. Instead, the apparent peak shear strength envelope at an elevated strain rate is assumed representative.

The input parameters that constitute the GCM is summarised in Table 1. Within this study, the input parameters for GCM are derived with respect to commonly used geotechnical parameters that arise from field and laboratory data; namely Cam-Clay for volumetric behaviour, and Mohr–Coulomb or Drucker–Prager for shear behaviour. This is so that the input can be readily determined from the various initial conditions reported from geotechnical site investigations of various civil earthworks projects.

Note: ρ is the mass density; K and G are the elastic bulk and shear moduli; α, θ, γ, and β are shear envelope parameters; R is the surface cap ratio; T is the tension cut off limit; X_0, D and W are hardening law parameters; $\bar{C}$ and $\bar{N}$ are kinematic hardening parameters.

2.2.1. Yield surface input

Within this study, $\gamma = \beta = 0$ is specified to reduce the shear failure envelope (F_e) to a linear Drucker–Prager criterion; where: d and M are respectively the Drucker–Prager cohesion and slope in the $p-q$ plane. Furthermore, as the Drucker-Prager parameters are related to their Mohr-Coulomb counterparts, effective cohesion (c') and the effective internal angle of friction (ϕ'), α and θ are calculatable by Eqs. (1) and (2).

$$\alpha = \frac{d}{\sqrt{3}} = \frac{18 \bullet c' \bullet \cos(\phi')}{\sqrt{3} \bullet (3 - \sin(\phi'))} \tag{1}$$

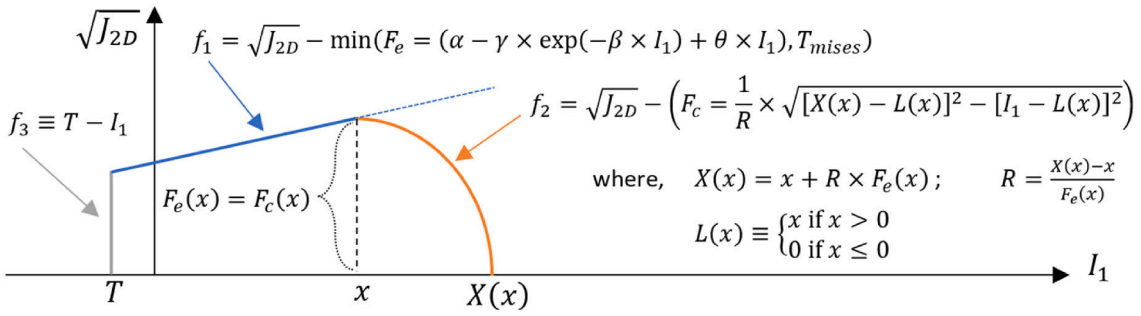

Fig. 2. Yield surface of Mat_025 in $\sqrt{J_{2D}} - I_1$ plane (after LSTC, 2015).

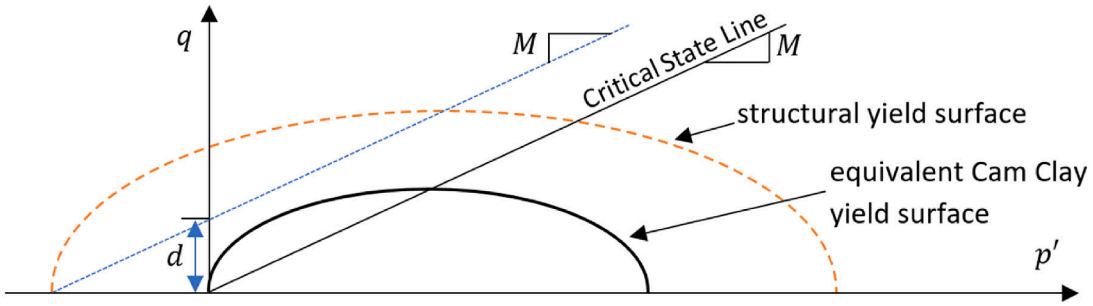

Fig. 3. Structural and equivalent yield surface in $p - q$ plane (after Liu, 2013).

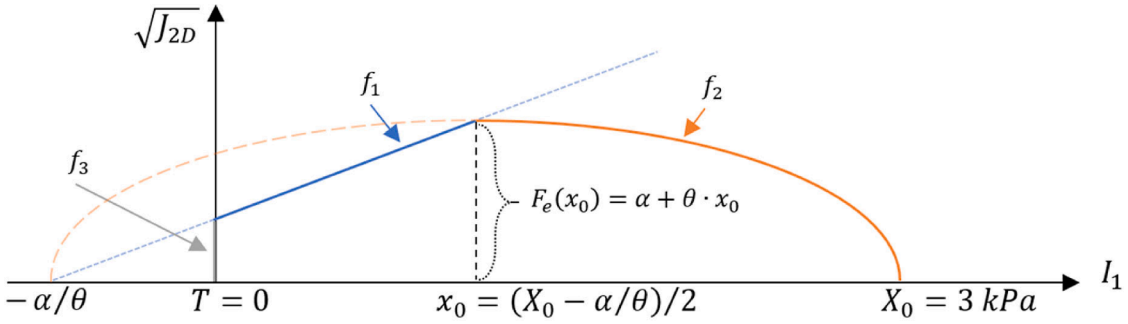

Fig. 4. Initial yield surface of the two-invariant cap model in $\sqrt{J_{2D}} - I_1$ plane.

$$\theta = \frac{M}{3\sqrt{3}} = \frac{2 \bullet \sin(\phi')}{\sqrt{3} \bullet (3 - \sin(\phi'))} \tag{2}$$

The initial cap surface, Fig. 2, is defined with respect to the shear failure envelope (f_1), the initial surface cap intercept along the I_1 axis ($X(x = x_0) = X_0$) and the surface cap ratio (R). Educated assumptions are necessary for X_0 and R. As the model represents a coarse-grained material, it is reasonable to assume the soil is effectively normally consolidated in its initial state. Hence, in this study, the initial cap surface intercept is assumed to reflect this: $X_0 = 3$ kPa (or 1 kPa mean pressure, p).

The estimation of R, and thereby the shape of the cap surface within this study, considers the cap yield surface to be similar to the wet side yield surface of the Structured Cam Clay model by Liu & Carter (2002) and Liu (2013), as shown in Fig. 3. Hence, given the failure envelope passes through the apex and mid-plane of the yield surface in the $p - q$ plane (Fig. 4), the surface cap ratio (R) is thus calculated from Eq. (3).

$$R = \frac{X_0 - x_0}{F_e(x_0)} = \frac{1}{\theta} = \frac{3\sqrt{3}}{M} = \frac{\sqrt{3} \bullet (3 - \sin(\phi'))}{2 \bullet \sin(\phi')} \tag{3}$$

2.2.2. Volumetric input

Within this study, the input parameters of GCM that define the volumetric strain of the material is determined by calibrating the total and elastic volumetric strains to the Cam Clay model's volumetric strains [Eqs. (4) to (9)]. Where, total volumetric strain of GCM ($\varepsilon_{v|GCM}$) is the sum of its elastic ($\varepsilon^e_{v|GCM}$) and plastic ($\varepsilon^p_{v|GCM}$) volumetric strains [Eqs. (6) and (7)]. The Cam Clay model volumetric strain ($\varepsilon_{v|CC}$), under monotonic loading, is by Eq. (8).

$$\int_{1\ kPa}^{p_{max}} \varepsilon_{v|\mathrm{GCM}}\, dp = \int_{1\ kPa}^{p_{max}} \varepsilon_{v|CC}\, dp \tag{4}$$

$$\int_{1\ kPa}^{p_{max}} \varepsilon^e_{v|\mathrm{GCM}} dp = \int_{1\ kPa}^{p_{max}} \varepsilon^e_{v|CC}\, dp \tag{5}$$

$$\varepsilon^e_{v|GCM} = \frac{p}{K} \tag{6}$$

$$\varepsilon^p_{v|\mathrm{GCM}} = W \bullet \{1 - \exp[-D \bullet (X(x) - X_0)]\} \tag{7}$$

$$\varepsilon_{v|CC} = \begin{cases} \dfrac{\kappa \bullet \ln(p)}{1 + e_0}, p < p_c \\ \dfrac{e_0 - e_L - (\kappa + \lambda) \bullet \ln(p)}{1 + e_0}, p \ge p_c \end{cases} \tag{8}$$

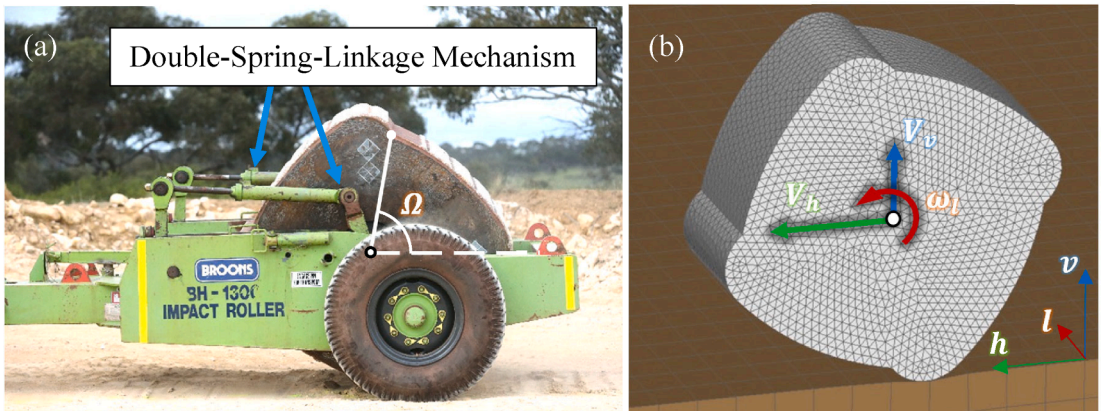

Fig. 5. Broons BH–1300, 4–sided, 8-t impact roller: (a) prototype; and (b) FE mesh.

$$\varepsilon^{e}_{v|CC} = \frac{\kappa \bullet \ln(p)}{1 + e_0} \tag{9}$$

Where: K is the elastic bulk modulus of the soil; p_c is the apparent preconsolidation pressure; e_0 is the initial void ratio of the soil ($at\ p = 1$ kPa); e_L is the intercept void ratio of the soil along the virgin compression line ($at\ p = 1$ kPa); κ is the logarithmic slope of the unloading–reloading line (URL); and λ is the logarithmic slope of the virgin compression line (VCL).

The calibration is undertaken from $p = 1$ kPa to an elected max pressure (p_{max}); where p_{max} must be greater than p_c. For this study, $p_{max} = 1.2$ MPa based off the peak vertical stresses measured in the field by Canala et al. (2014) and Scott et al. (2019a, 2019b), and prior numerical estimates by Kim (2010), Bradley et al. (2012) and Kuo et al. (2013).

As W is the limit of $\varepsilon^{p}_{v|GCM}$, it is taken to be $\varepsilon^{p}_{v|CC}$ at p_{max} [Eq. (10)]. As a consequence of Eqs. (4) to (10), K and D are calculated by Eqs. (11) and (12); where $W_z(\bullet)$ is the Lambert W Function, and recall: $X_0 = 3\ kPa$. Noting GCM's elasticity follows the generalised Hooke's law, the elastic shear modulus (G) is calculated following the elastic moduli relationships [Eq. (13)].

$$W = \frac{\lambda - \kappa}{1 + e_0} \bullet \ln\left(\frac{p_{max}}{p_c}\right) \tag{10}$$

$$K = \frac{\left(p^2_{max} - 1\right) \bullet (1 + e_0)}{2(\kappa + (\kappa \bullet p_{max} \bullet (\ln(p_{max}) - 1)))} \tag{11}$$

$$G = \frac{3 \bullet K \bullet (1 - 2 \bullet \nu)}{2 \bullet (1 + \nu)} = \frac{3 \bullet K \bullet E}{9 \bullet K - E} \tag{13}$$

2.3. Roller model

As shown in Fig. 5, the Broons BH–1300, 4–sided, 8-tonne impact roller module was modelled using 1–point tetrahedral elements (ELFORM = 10) and incorporates 22,216 nodes.

As the 4-sided roller is solely connected to the trailer chassis via the double-spring-linkage mechanism [Fig. 5(a)], the roller's motion is non-trivial. As a result, to honour the module's rotational and horizontal motion in the field, the roller's motion is semi–constrained in the model. Consistent with the plane of symmetry, the roller is fixed in translation along the lateral l–axis, and rotation about the forward horizontal h-axis and rotation about the vertical ν- axis. For the static case, the roller has degrees of freedom along and about all other axes. For the dynamic case, during each pass, the forward horizontal velocity of the roller (V_h) and the angular velocity about its axle (ω_l), are prescribed to their respective *typical motion* time histories ($\widehat{V}_x, \widehat{\omega}_x$) by Bradley et al. (2019). The vertical velocity (V_v) is prescribed as a degree of freedom to be calculated by the model. This allows the modelled roller to account for an evolving surface condition, permit a degree of variability in the roller's behaviour, and act as a cross–check on the model reproducing an approximation of the *typical motion* vertical velocity ($\widehat{V}_y$) time history by Bradley et al. (2019).

At initialisation, the angular orientation of the roller (Ω) [Fig. 5(a)], $\Omega = 24^{\circ}$ for the static case, and for the dynamic case $\Omega = 0^{\circ}$. Additionally, for the dynamic case, care is taken to ensure that, at the start of each pass, $\Omega = 0^{\circ}$ by end of the resetting phase. Further details of the

$$D = \frac{(\Gamma) \bullet \left(p^2_{max} + 6 \bullet K \bullet W \bullet p_{max} - 6 \bullet \xi \bullet K - 2 \bullet K \bullet W \bullet X_0 - 3\right) + (2 \bullet K \bullet W) \bullet \left(3 \bullet p_{max} - X_0\right)}{\left(3 \bullet p_{max} - X_0\right) \bullet \left(3 \bullet p^2_{max} + 6 \bullet K \bullet W \bullet p_{max} - 6 \bullet \xi \bullet K - 2 \bullet K \bullet W \bullet X_0 - 3\right)}$$

$$,\xi = \frac{1}{1 + e_0}\begin{pmatrix} \kappa + (\kappa \bullet p_c) \bullet \left(\ln(p_c) - 1\right) + (p_{max}) \bullet \left(\lambda \bullet \ln(p_{max}) - \lambda - e_L + e_0\right) \\ -(p_c) \bullet \left(\lambda \bullet \ln(p_c) - \lambda - e_L + e_0\right) \end{pmatrix}$$

$$,\Gamma = W_z\left(-\frac{(2 \bullet K \bullet W) \bullet \left(3 \bullet p_{max} - X_0\right) \bullet \exp\left[\frac{-(2 \bullet K \bullet W) \bullet \left(3 \bullet p_{max} - X_0\right)}{3 \bullet p^2_{max} + 6 \bullet K \bullet W \bullet p_{max} - 6 \bullet \xi \bullet K - 2 \bullet K \bullet W \bullet X_0 - 3}\right]}{3 \bullet p^2_{max} + 6 \bullet K \bullet W \bullet p_{max} - 6 \bullet \xi \bullet K - 2 \bullet K \bullet W \bullet X_0 - 3} \right) \tag{12}$$

Table 2
Summary of geotechnical parameters for sandy gravel fill material.

USCS	ρ_0 (t/m^3)	$\rho_{d\|0}$ (t/m^3)	G_s (t/m^3)	e_0	e_{max}	e_{min}*	Dr_0 (%)	e_L	p_c (kPa)	κ	λ	c' (kPa)	ϕ'_{cv} (°)	d (kPa)	M
GP	1.880	1.675	2.654	0.585	0.816	0.328	47.4	0.850	197	0.0035	0.0537	13.5	38.5	80	1.57

Note: * - based upon modified Proctor test (Standards Australia, 2017)

resetting phase are given in Section 2.4 below.

Considering the rigidity of the material properties of the roller relative to that of the soil, a rigid material model (Mat_020) is used to define the roller as rigid. The properties of the roller are assumed as follows: total mass of the half–roller is 4 tonnes, $E = 5$ GPa and $\nu = 0.2$.

The contact definition between the roller and the soil body is defined by a soft constraint formulation (i.e. *CONTACT_AUTOMATIC_SURFACE_TO_SURFACE). In the absence of a more precise understanding, the algorithm's friction parameters that define the coefficient of friction (μ) is assumed to be velocity independent and is the tangent of the soil's internal angle of friction (ϕ'), such that $\mu = FS = FD = \tan(\phi')$; where, FS and FD are the static and dynamic coefficients of friction, as similarly assumed by Kim (2010) and Bastaee & Parvizi (2012). Although the friction between the roller and soil is unlikely to be velocity independent, it is an acceptable practice in the absence of data for velocity dependency (LSTC, 2015). Additionally, by simplifying the algorithm, computer demands are reduced, thus allowing for a more time efficient model.

The typical approach within the literature (Kim, 2010; Bastaee & Parvizi, 2012) is that the roller's loading be derived by its mass inertia alone. However, in the field, additional loading is provided by the double–spring–linkage mechanism. Clifford & Bowes (1995) stated the double-spring-linkage mechanism contributes to the roller fall speed, increasing it by 10 to 20%. It is reasonable to suggest that this contribution is implicitly included within the *typical motion* time histories by Bradley et al. (2019). However, as vertical velocity (V_v) is specified as an unconstrained degree of freedom, an additional vertical loading is likely to be needed to account for the additional loading provided through the double-spring-linkage mechanism.

Moreover, the contact interaction between the roller and the soil is subject to error. Particularly, given the motion is semi–constrained, thereby the accumulation of errors from misaligned synergies between the surface conditions and the prescribed motion will arise in V_v.

Hence, an additional constant downward vertical loading (L) is prescribed to each of the 22,216 nodes that form the roller. Three values are considered: (1) $L = 0$ N; (2) $L = 0.25$ N; and (3) $L = 1$ N, where, $L = 0.25$ N represents an additional vertical static load of about 14%, which is consistent with that suggested by Clifford & Bowes (1995). Whilst $L = 0$ N and $L = 1$ N represent a lower and upper bound estimate.

2.4. Modelling multiple passes

RDC involves improving the ground by performing multiple passes of the non–cylindrical roller within a target lane. The implementation of a

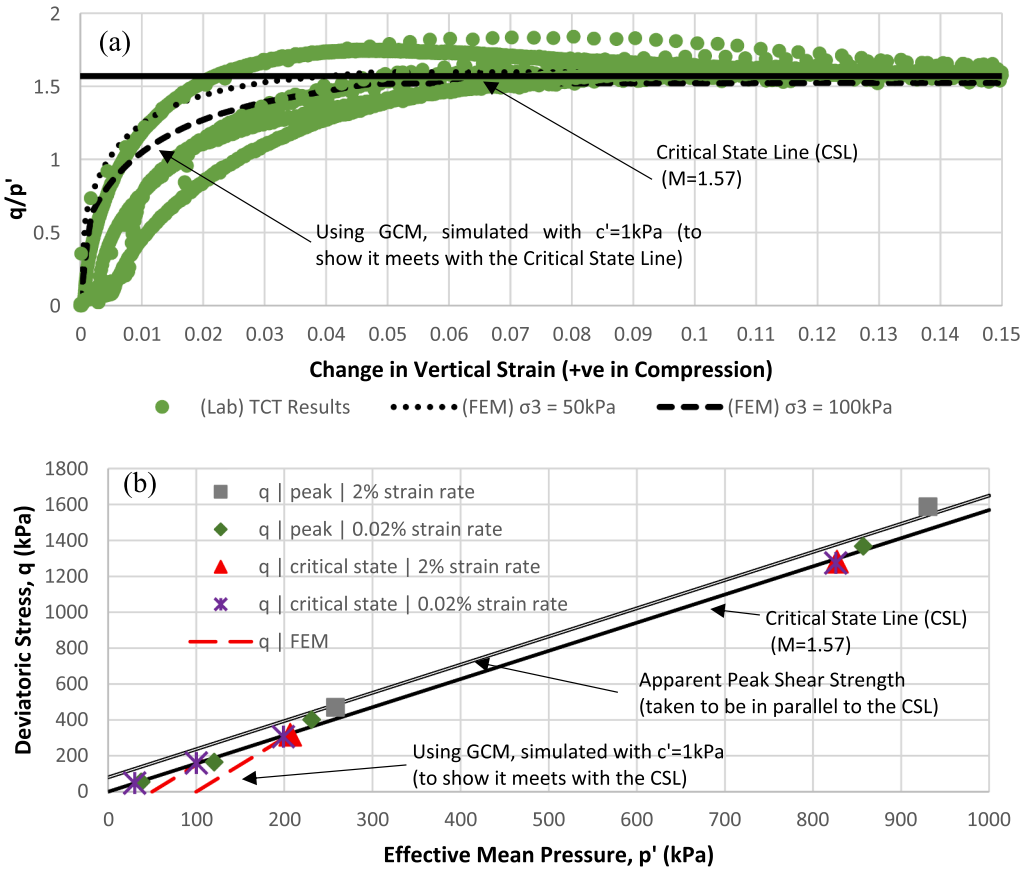

Fig. 6. Summary of laboratory shear strength tests (with simulations using GCM): (a) ratio of deviatoric stress to effective mean pressure against vertical strain; and (b) deviatoric stress against effective mean pressure.

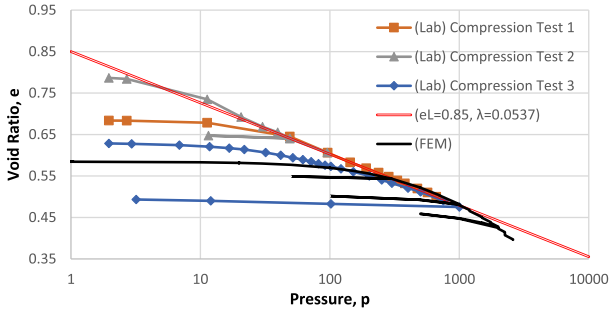

Fig. 7. Summary of laboratory compression tests (with a simulation using GCM).

multiple pass scenario within the FE model is such that after the roller has undertaken its 10th impact along the lane, concluding its pass, the roller begins a resetting phase to prepare the roller and lane for the next pass. The resetting phase consists of: (1) the roller is lifted clear above the soil body following the 10th impact as the roller reaches its apex height ($\Omega = 81 \sim 90^{\circ}$); (2) the roller is re-oriented to $\Omega = 0^{\circ}$ whilst it is brought back some distance, to the beginning of the lane; (3) the roller is gently brought down to 100–200 mm above the soil surface before being released/dropped on to the soil surface; (4) time is permitted for the roller to interact and dampen with the soil body before re–engaging the semi–constrained *typical motion* $(\widehat{V}_x, \widehat{\omega}_x)$ as it begins its next pass. The offset to which the roller is drawn back to, along the *h*-axis, following the i^{th} pass, is denoted r_i (see Fig. 1), such that $r_i = 100$ mm would reposition the roller, following the i^{th} pass, to 100 mm behind the roller's initial position at the start of the transient phase ($time = 0$). The offset for each pass is adjusted such that the disturbance experienced through the resetting phase is mitigated, and the V_v produced is in reasonable agreement with the typical $\widehat{V}_y$ time history by Bradley et al. (2019).

3. Field Trial

A field trial of the BH–1300, 8 tonne, 4–sided impact roller was undertaken on a 12 × 7.5 m test bed at Monarto Quarry, which is approximately 60 km south of Adelaide, Australia. The test bed was excavated to 1.5 m depth and backfilled with a local sandy gravel fill material; the same fill material and methodology consistent with the field investigations of Scott et al. (2016, 2019a) and Bradley et al. (2019). A natural gravelly sand, of medium-dense consistency, underlies the test bed. The test bed was sub–divided into three, adjacent, 2.5 m wide lanes, identified as lanes A, B, and C, and each subjected to 5, 10 and 30 passes of the roller towed at 10 km/h, respectively.

3.1. Material properties

To obtain the appropriate input parameters for the numerical modelling of the soil, a series of laboratory tests was performed on the fill material used in the test bed. A summary of the geotechnical properties of the fill material is presented in Table 2, with the corresponding GCM inputs in Table 1. In general, the physical properties of the fill material are within expectations and are consistent with measurements by Hosseini et al. (2005) of similar material.

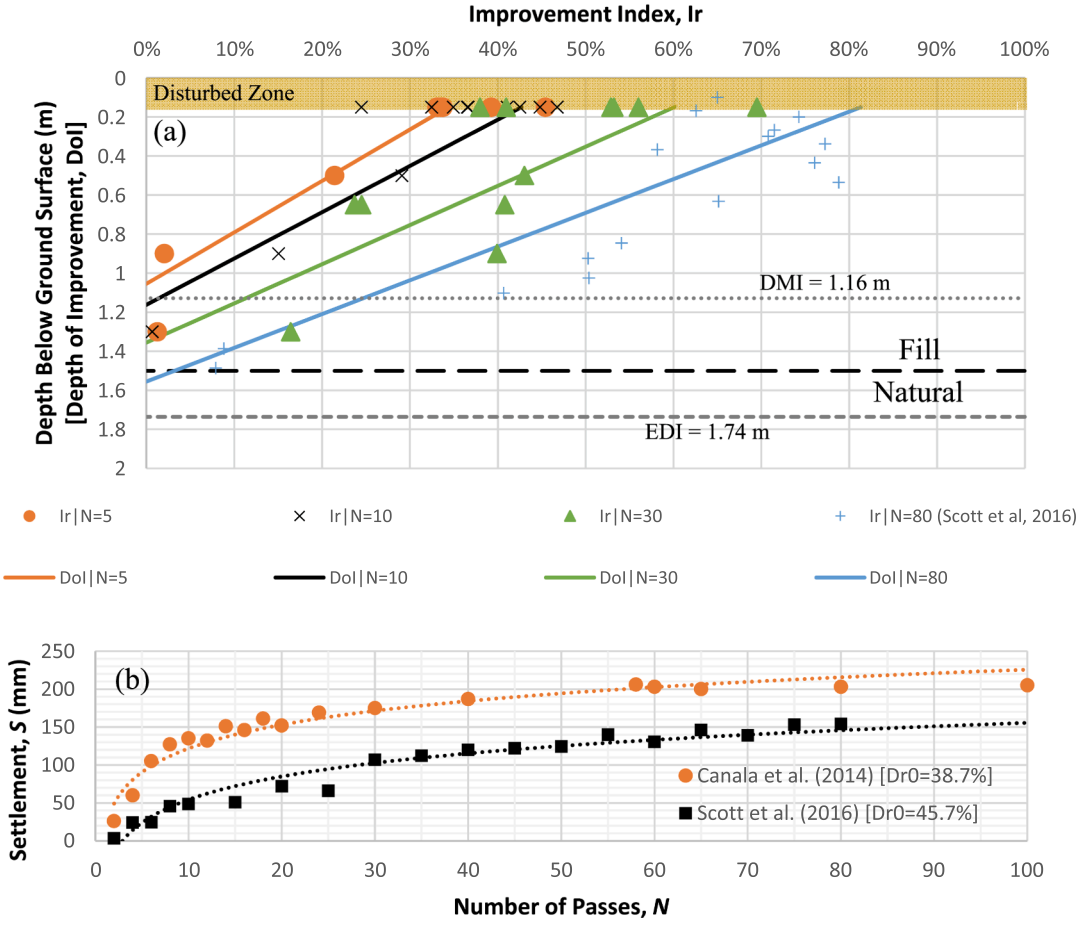

Fig. 8. Summary of field results: (a) compaction; and (b) settlement data.

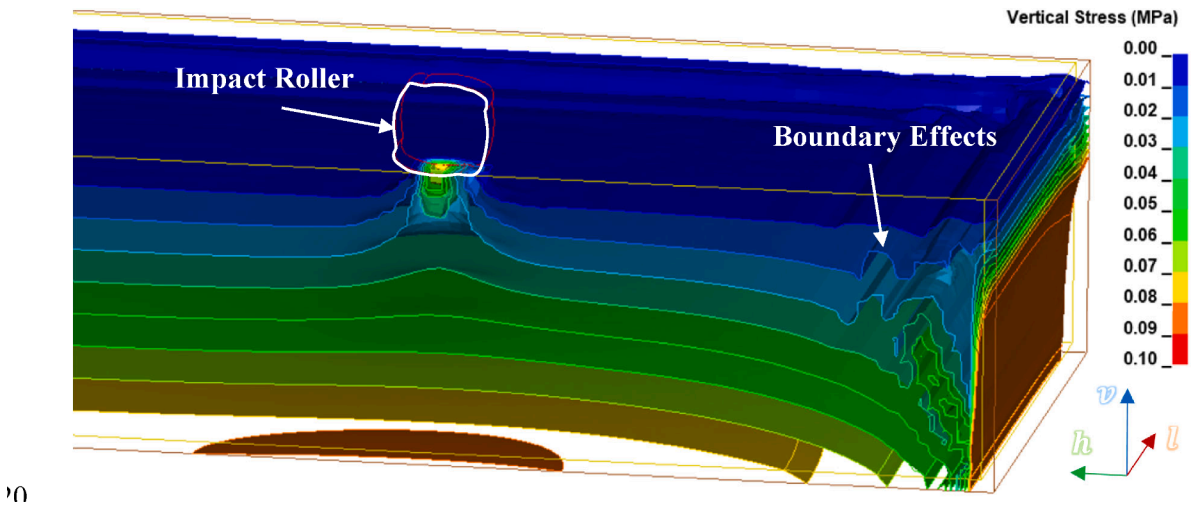

Fig. 9. Vertical stress underneath the impact roller at conclusion of the dynamic relaxation for the static case.

Particle size distribution tests (Standards Australia, 2009) on bulk samples of the fill material report a maximum particle size of no greater than 20 mm and is described as a poorly-graded sandy gravel with a trace of fines by the Unified Soil Classification System (USCS). Informed by a combination of dynamic cone penetration (DCP) (Standards Australia, 1997) and nuclear density meter testing (Standards Australia, 2007), the initial density (ρ_0) and initial dry density $(\rho_{0|d})$ of the fill, prior to RDC, the soil was reasonably homogenous throughout the lift. The specific gravity of the solids (G_s) of the fill material was estimated from 11 pycnometer tests (Standards Australia, 2006). The maximum void ratio (e_{max}) of the fill material was estimated as per AS 1289.5.5.1 (Standards Australia, 1998) and the minimum void ratio (e_{min}) of the fill material is selected as that associated with the maximum dry density from the modified Proctor test (Standards Australia, 2017). Hence, for a given dry density (ρ_d), the void ratio (e), and relative density (Dr) are thus calculated from Eqs. (14) and (15).

$$e = \frac{G_s}{\rho_d} - 1 \tag{14}$$

$$Dr = \frac{e_{max} - e}{e_{max} - e_{min}} \tag{15}$$

As presented in Fig. 6, consolidated undrained triaxial compression tests (Standards Australia, 2016) were undertaken at varying confinements, and strain rates, to identify the critical state effective angle of friction (ϕ'_{cv}) and the apparent peak effective cohesion (c') of the fill

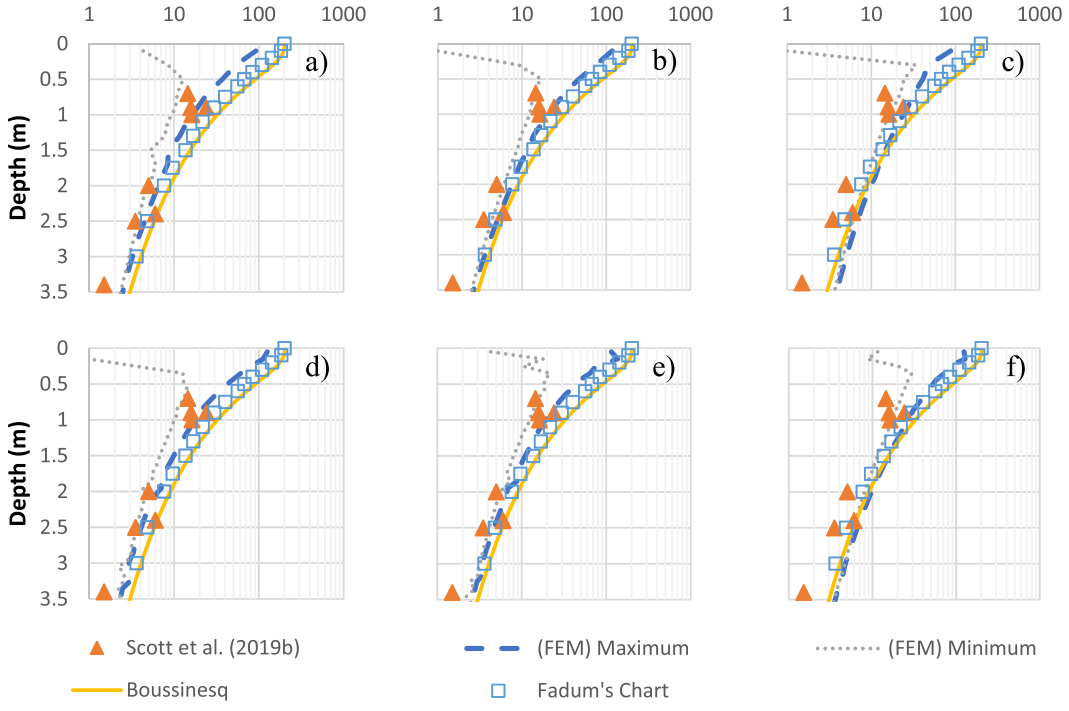

Fig. 10. Vertical applied stress, σ_V^A (kPa), beneath the 8–tonne 4–sided roller for the static case: (a) L = 0 N/node [200 × 200 × 200 mm]; (b) L = 0.25 N/node [200 × 200 × 200 mm];(c) L = 1 N/node [200 × 200 × 200 mm]; (d) L = 0 N/node [100 × 100 × 100 mm]; (e) L = 0.25 N/node [100 × 100 × 100 mm] (f) L = 1 N/node [100 × 100 × 100 mm].

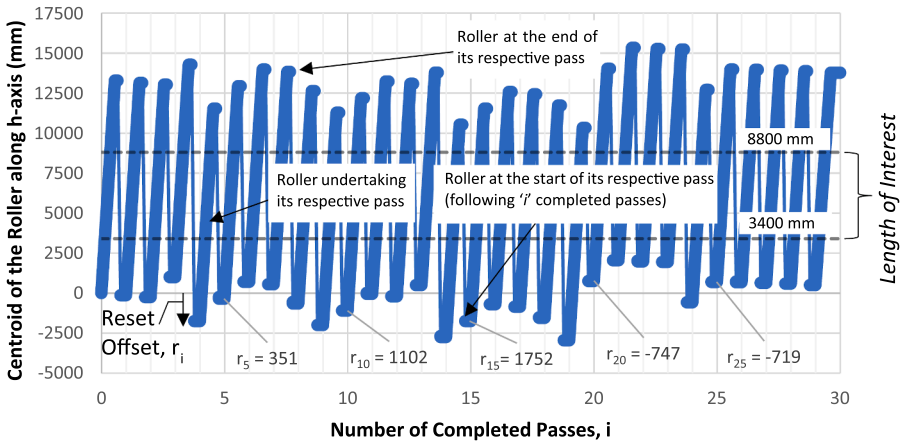

Fig. 11. Resetting regime of the roller along the lane for the dynamic analyses.

material. The apparent peak shear strength envelope, and thereby c', is estimated by fitting the peaks of the tests subject to an elevated strain rate whilst maintaining a slope parallel to the critical state line. Therefore, the strength gain due to an elevated strain rate, as we would expect through the action of impact, is represented modestly. The volumetric behaviour of the fill material was investigated with 1D-compression tests (Standards Australia, 2020), the results of which are given in Fig. 7. The tests were undertaken at varying initial densities and loaded to a maximum mean pressure of 1 MPa. Thereafter, to assess the veracity of the GCM and its inputs, simulations of the laboratory (triaxial compression and 1D-compression) tests were undertaken. The simulations, as presented in Figs. 6 and 7, show good agreement with the laboratory test data.

3.2. Field trial results

In relation to RDC, the change in density is adopted as the key indicator of improvement with respect to depth and the number of passes. This was estimated from a combination of DCP and nuclear density meter testing to measure density at depth; prior to RDC and post RDC.

Fig. 8 presents a summary of the results of the field trial, and also incorporates the settlement measurements from Canala et al. (2014) and Scott et al. (2016), who as mentioned previously, also performed field trials, involving 100 and 80 passes, respectively, using the same material as that presented in Section 3.1. However, it should be noted that Canala et al. (2014) did not maintain a consistent speed for all 100 passes as they conducted their investigation with respect to varying towing speeds (5–16 km/h). Whereas Scott et al. (2016) maintained a consistent speed and had an initial relative density (D_{r0}) akin to the field trial presented herein. The results are presented in terms of the at depth improvement index (I_r) [Eq. (16)] and the surface settlement (S) with respect to the number of passes (N).

The upper 150 mm is typically disturbed, which is consistent with the findings of others (e.g., Clifford 1975, 1978; Ellis 1979; Scott & Jaksa 2014, 2015; Scott et al. 2016), where it is not uncommon for the upper 300 mm to be disturbed due to shearing action and the formation of an undulating surface profile. Below the disturbed near surface soils, a trend between I_r for a given depth of improvement (DoI) and N [Eq. (17)] is identified. For comparison, the effective depth of improvement (EDI) and depth of major improvement (DMI) for the field test, as defined by Scott et al. (2019b), is estimated to be 1.74 m and 1.16 m, respectively. Additionally, the settlement data from Canala et al. (2014) and Scott et al. (2016) suggests a natural logarithmic trend with respect to N.

$$I_r = \frac{D_r - D_{r0}}{1 - D_{r0}} \tag{16}$$

$$\widehat{I}_{r\,field} = \frac{0.8418 \bullet N^{0.1401} - DoI}{3.3640 \bullet N^{-0.1520}} \tag{17}$$

where $N \geq 5$ passes; $100\% \geq \widehat{I}_{r\,field} \geq 0\%$; $DoI \geq 0.15$ m

4. Numerical Modelling

This section presents the results of the numerical modelling. Firstly, to calibrate and validate the model, the static case is discussed, and the dynamic analyses are subsequently presented.

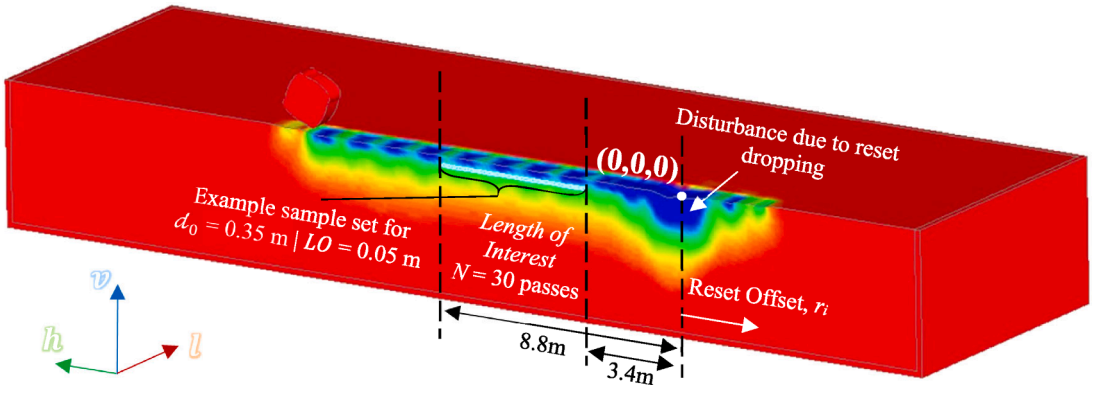

Fig. 12. Dynamic case FE model after 30 passes (illustrating the general extent of resulting vertical displacement across the model).

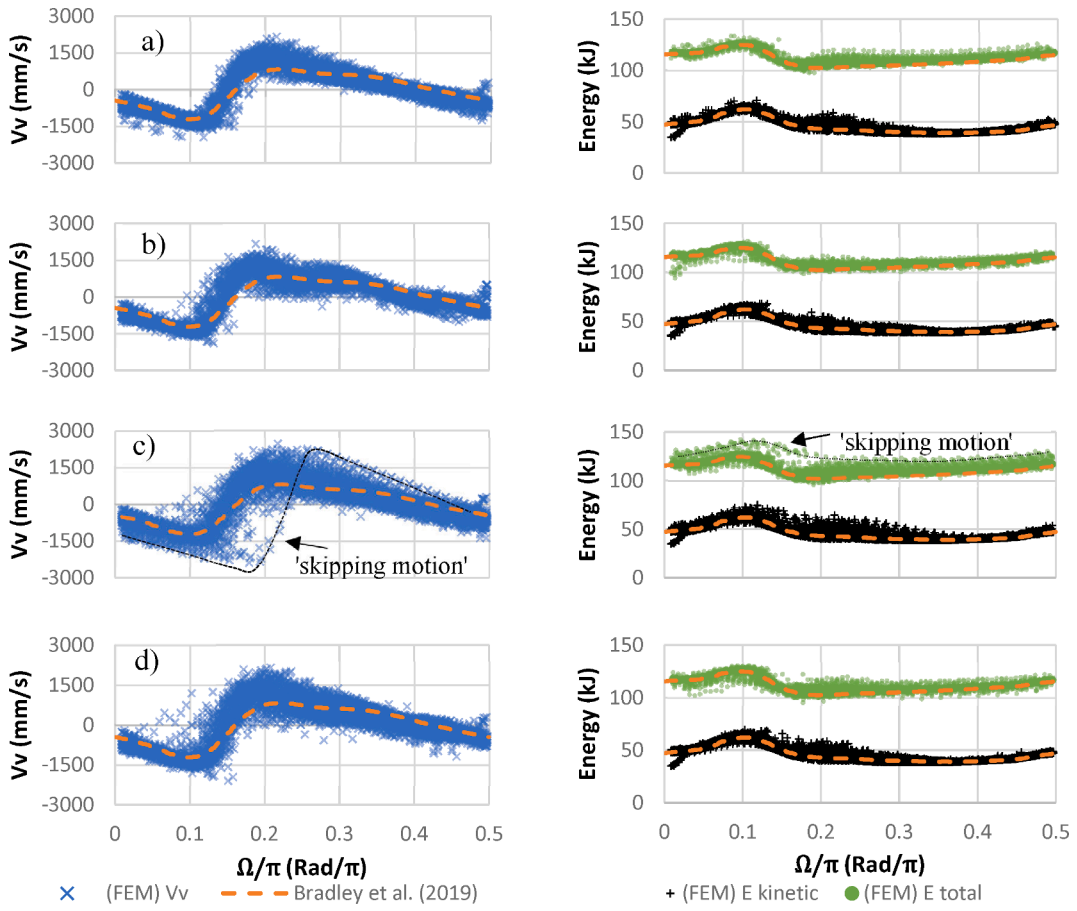

Fig. 13. Summary of V_v, total energy, and kinetic energy from the FE simulations: (a) L = 0.25 N/node [200 × 200 × 200 mm]; (b) L = 1 N/node [200 × 200 × 200 mm]; (c) L = 0.25 N/node [100 × 100 × 100 mm] (d) L = 1 N/node [100 × 100 × 100 mm].

4.1. Static Case Results

Fig. 9 shows the static weight of the roller resting on the soil surface, clear of boundary effects. The applied vertical stress $(\sigma_V^A = \sigma_V - \sigma_{V0})$, the total vertical stress less the initial overburden, estimated by Scott et al. (2019a, 2019b), in addition to that predicted using Boussinesq's (1885) formulation for a circular (0.35 m radius) foundation (Bowles, 1997) and Fadum's chart (Knappett & Craig, 2012) for a rectangular (1.3 × 0.3 m) foundation are used to benchmark the FE model for the static case. The maximum and minimum σ_V^A beneath the roller using FEM, with respect to $L = 0, 0.25, 1$ N/node, using either a fine (100 × 100 × 100 mm) or coarse (200 × 200 × 200 mm) FE mesh, is presented in Fig. 10.

As can be seen, there is very good agreement between all estimates in Fig. 10. As expected, the finer mesh provides a more accurate representation and permits an increased maximum stress to be realised. However, although marginally, $L = 0$ underrepresents the stress applied to the soil. This in turn suggests that a nominal additional vertical load is necessary to overcome the limitations of the contact interaction between the roller and the soil, and account for loads in addition to the module's self-weight. Concerning the additional loadings, the upper value of $L = 1$ N/node appears to be less applicable when compared to the lower $L = 0.25$ N/node for the static case. Given the magnitude of the upper loading, this is expected, however it provides confidence in the lower value being a necessary minimum inclusion in the FE model. In the dynamic analyses that follow, $L = 0$ is not considered further.

4.2. Dynamic Case Results

A total of four dynamic analyses are performed, all involving 30 passes of the BH–1300, 8 tonne, 4–sided impact roller. To examine the effect of mesh size on the predictive performance of the numerical model, a fine (100 × 100 × 100 mm) and coarse (200 × 200 × 200 mm) soil mass FE mesh is used. In addition, the influence of the applied vertical load, L, of 0.25 and 1 N per node, is also examined. For each of the completed passes (i), the adopted reset offset (r_i) for each pass is illustrated in Fig. 11.

Since r_i is non–zero, and the roller performs 10 impacts per pass, the roller does not perform all 30 passes across the full length of the lane. In fact, as shown in Fig. 11, the roller performs all 30 passes for approximately 8.2 m along the lane. Further, the roller is kept clear of the boundary so to mitigate boundary effects. As shown in Figs. 11 and 12, the inner 5.4 m, is taken as the *length of interest* that is considered for the assessment of the influence of RDC in the numerical model. This is to ensure that adjacent roller impacts are appropriately considered.

As shown in Fig. 12, in each of the simulations, an accumulation of vertical displacement (or disturbance) produced at the start of the lane consistently occurred in the vicinity of the reset drop locations. This is even though the reset locations were distributed across approximately 5 m. Although the disturbance is present, it is sufficiently separated from the *length of interest* to have no effect on the results obtained.

In the sub-sections that follow, firstly, the kinematics of the roller are examined in Section 4.2.1, to confirm the roller's motion and the magnitude of energy delivered to the soil is consistent with the *typical motion* observed in the field by Bradley et al. (2019). Subsequently, in Section 4.2.2, the resulting ground settlement along the 5.4 m *length of interest* is examined. Finally, in Section 4.2.3, the densification of the soil

Table 3
Summary of resulting energy characteristics through each impact.

Mesh Resolution (mm)	L (N/node)	$E_{kinetic}^{peak}$ (kJ)[1]	E_{lost} (kJ)[1]	$E_{absorbed}$ (kJ)[1]
200 × 200 × 200	0.25	63.6 ± 0.2	21.1 ± 0.6	19.4 ± 1.0
	1	63.3 ± 0.2	21.0 ± 0.6	19.4 ± 0.8
100 × 100 × 100	0.25	63.6 ± 0.3	22.1 ± 1.1	20.9 ± 2.1
	1	63.5 ± 0.2	21.6 ± 0.6	20.6 ± 1.4

Note[1]: at 95% confidence.

is assessed along the lane with respect to initial depth ($\measuredangle_0$) and lateral offset distance from the centreline of the lane (LO).

4.2.1. Roller motion and energy delivered

Fig. 13 presents the numerical model results, performed at 40 Hz, of the vertical velocity (V_v), the kinetic energy and the total energy time histories of the roller for all 10 impacts for each of the 30 passes, with respect to the angular orientation of the roller (Ω) [see Fig. 5(a)]. These are benchmarked against field observations reported by Bradley et al. (2019). For the most part, all four of the FE simulations reproduced behaviour consistent with field observations of the kinematics of the BH–1300, 8 tonne, 4–sided impact roller. This is despite adopting a consistent resetting regime, Fig. 11, between each dynamic analysis. However, some discrepancies in the motion are observed. Namely, there is a distinct increase in the variability of the motion with respect to the FE mesh resolution. Though this is not unexpected given the interaction between the roller and the soil is dependent on the resolution of the FE mesh.

Further, a single event of 'skipping motion' [Fig. 13(c)], where the roller is not engaging in *typical motion* was produced. The roller instead behaved more akin to the non–uniform rotation and skipping behaviour as observed at elevated towing speeds of 13 km/h and higher by Scott et al. (2020). If greater conformity to *typical motion* is desired, a refinement of r_i, and/or an increase in L, would reduce this variability. Nevertheless, all four simulations exhibit good agreement with that observed in the field.

The peak kinetic energy of the roller per impact $\left(E_{kinetic}^{peak}\right)$ is maintained between the simulations and agrees well with that reported by Bradley et al. (2019) and estimated by Clifford & Bowes (1995). Interestingly, averaged per pass, estimates for the energy absorbed by the soil body per impact ($E_{absorbed}$) is not necessarily the same as the energy of the roller lost per impact (E_{lost}); when they are expected to be approximately equal to one another, Table 3. A likely explanation is the fact that the motion of the roller, within the model, is semi–constrained. As the roller's horizontal velocity (V_h) and the angular velocity about its axle (ω_l) are prescribed, so too is their contribution to the kinetic energy of the roller in addition to any error that may be produced by the interaction

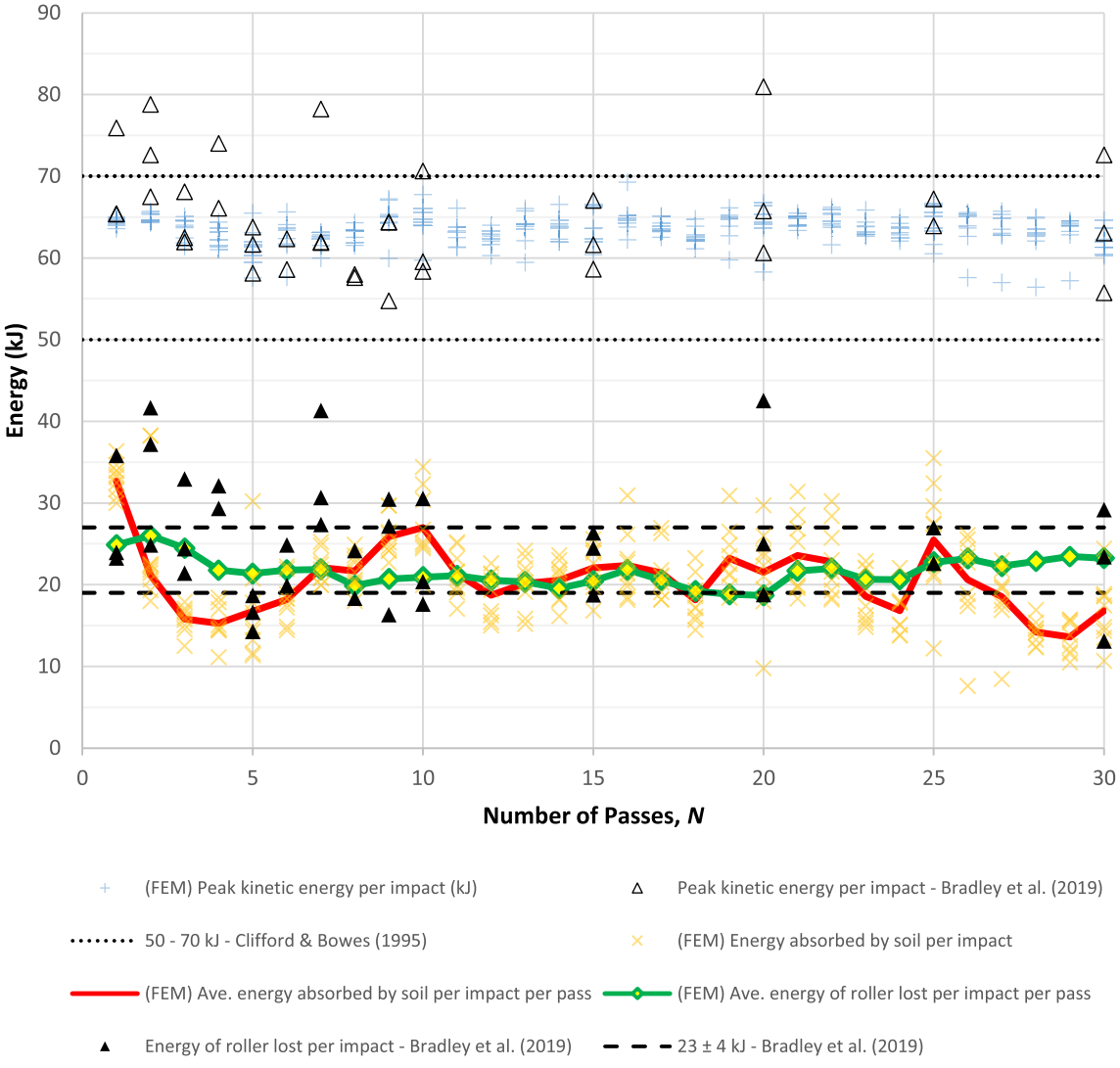

Fig. 14. Summary of FE roller's energy characteristics through each impact per pass: [using $L = 1$ N/node, 100 × 100 × 100 mm FE mesh].

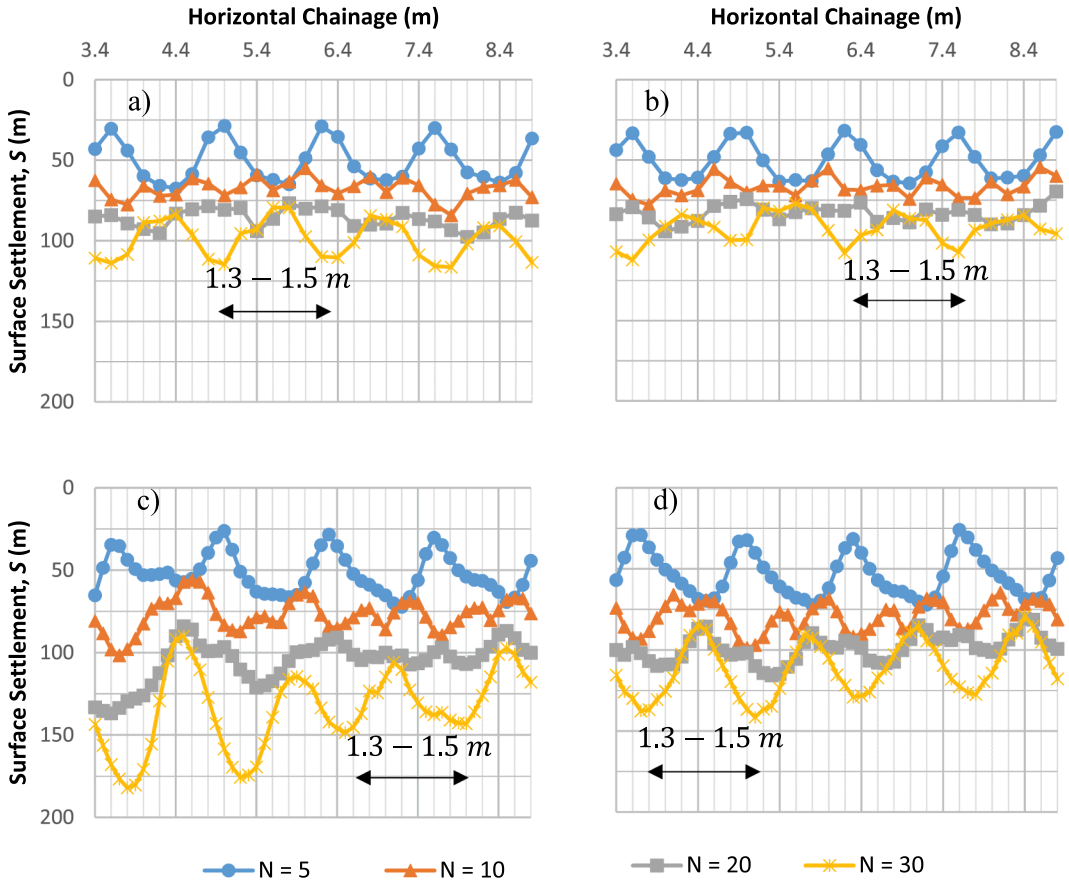

Fig. 15. Evolution of the undulating ground surface from the FE model: (a) L = 0.25 N/node [200 × 200 × 200 mm]; (b) L = 1 N/node [200 × 200 × 200 mm]; (c) L = 0.25 N/node [100 × 100 × 100 mm]; (d) L = 1 N/node [100 × 100 × 100 mm].

between the roller and soil with each impact. It is therefore possible that the prescribed gain/loss in motion, and thereby energy, are maintained for E_{lost} but do not necessarily align with the energy transmitted to and absorbed by the soil, effectively stiffening or softening the impact, attributing to circumstances in which $E_{absorbed} > E_{lost}$ and vice-versa. Nevertheless, the energy characteristics within the model are still in good agreement with that observed in the field. An example of how these energy characteristics present with respect to the number of passes is presented in Fig. 14.

As expected, the kinematics of the roller fit closer to *typical motion* as the magnitude of L increases. This is due to L providing an idealised account of the contribution of load provided by the double-spring-linkage mechanism. In addition, and as expected, the finer FE mesh resolution facilitated a greater magnitude of energy to be absorbed by the soil; suggesting that a discretization error may be present. Nevertheless, the resolution of either FE mesh is sufficient, although the finer FE mesh provides greater accuracy.

4.2.2. Surface undulations and settlement

The use of the 4-sided impact roller results in an undulating surface profile which evolves with each pass. The surface settlement, as estimated by the FE model, along the centreline of the roller's path, for $N = 5, 10, 20, 30$ passes, is presented in Fig. 15. The FE model reproduced the undulating ground surface and the manner by which it evolves with each successive pass. Further, the length of the imprint, measured base to base, made by the impact roller that forms the undulating surface, can be estimated. Produced by the FE model, after 30 passes, the imprint ranges between 1.3 and 1.5 m, which agrees well with the 1.4–1.6 m (for towing speed of 10 km/h) reported by Scott et al. (2020) in their field study incorporating varying towing speeds of the impact roller on a similar fill material.

Fig. 16 presents the range of ground settlement along the *length of interest*, with respect to each pass, compared with those reported by Canala et al. (2014) and Scott et al. (2016). The estimates appear reasonable, although potentially over-estimating the settlement with decreasing L. This is likely due to there being a tendency for more variable motion with decreasing L. Nevertheless, the general trend of the magnitude of settlement is in good agreement with that reported by Scott et al. (2016).

4.3. Compaction

At the conclusion of each pass, the magnitude of compaction is estimated along the *length of interest* and expressed in terms of I_r [Eq. (16)]. Note within this study $I_r = 100\%$ represents compacting the soil to the maximum dry density of the soil from a modified Proctor test (Standards Australia, 2017). Further, $I_r > 100\%$ represents compacting the soil beyond that achieved from a modified Proctor test, indicating a greater amount of compactive effort.

As shown in Fig. 17(b), the improvement along the centreline of the roller's path ($LO = 0.05$ m) is seemingly cyclical. Particularly at shallow depths, such as that shown for $z_0 = 0.35$ m, a significant range of I_r is produced. This is likely a natural outcome of the disturbance of the upper soils, whilst the roller impacts at regular intervals and is affected by the evolving undulating surface profile, thus compacting the soil likewise at regular intervals. To characterise the range of improvement

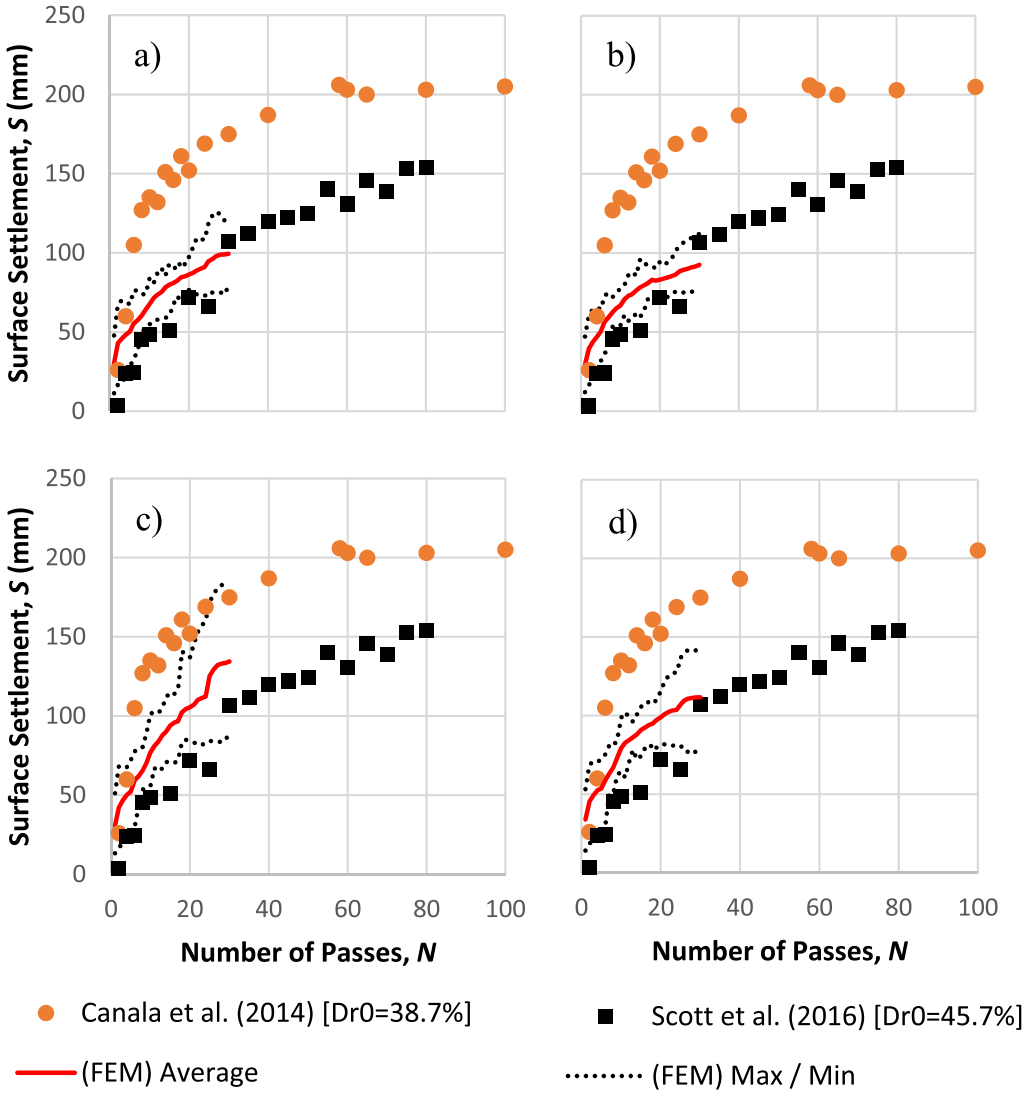

Fig. 16. Summary of FE model surface settlement: (a) L = 0.25 N/node [200 × 200 × 200 mm]; (b) L = 1 N/node [200 × 200 × 200 mm]; (c) L = 0.25 N/node [100 × 100 × 100 mm]; (d) L = 1 N/node [100 × 100 × 100 mm].

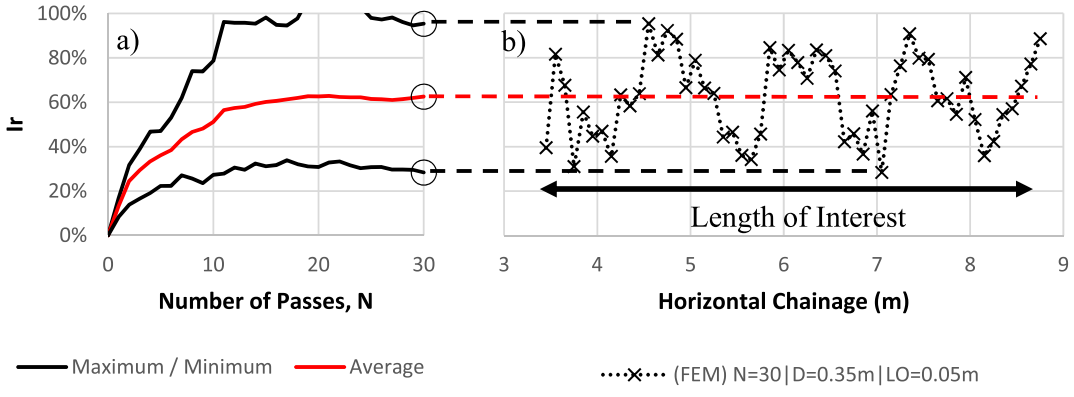

Fig. 17. Range of I_r for $\mathcal{L}_0$ = 0.35 m, and LO = 0.05 m: (a) with respect to N; (b) with respect to forward horizontal chainage (N = 30) [using L = 1 N/node, 100 × 100 × 100 mm FE mesh].

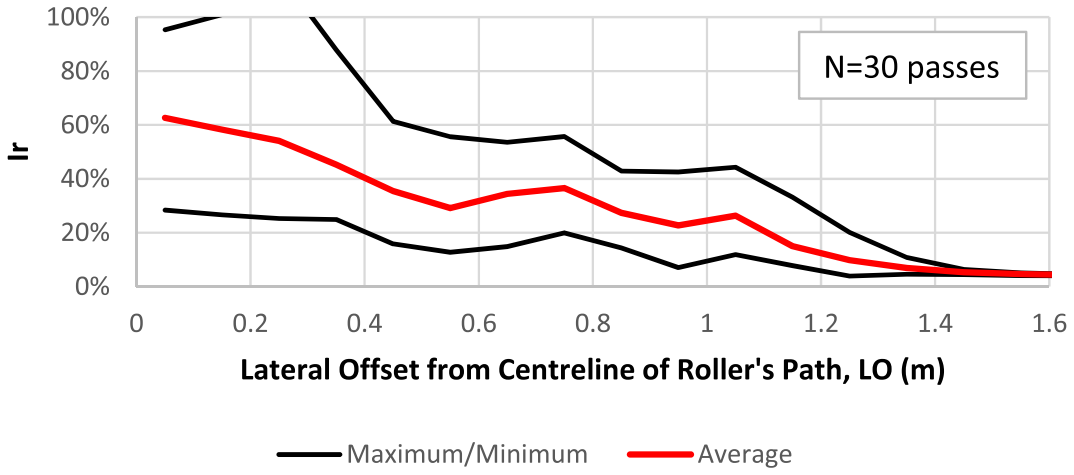

Fig. 18. Range of I_r for $\mathscr{d}_0 = 0.35$ m, N = 30, with respect to LO [using L = 0.25 N/node, 100 × 100 × 100 mm FE mesh].

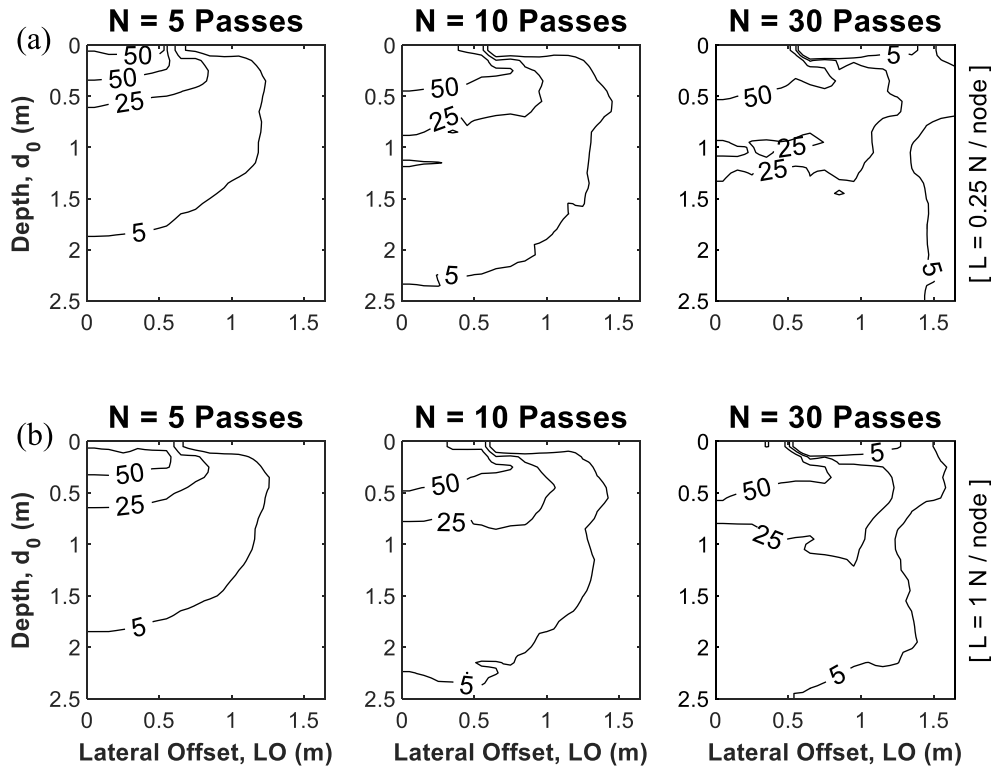

Fig. 19. Iso-curve cross sections of $I_{r|\max|N|\mathscr{d}_0|LO}$ for N = 5, 10, 30 Passes: [using 100 × 100 × 100 mm FE mesh] (a) $L = 0.25$ N/node; and (b) $L = 1$ N/node.

along the lane, the maximum $(I_{r|\max})$, average $(I_{r|\text{ave}})$, and minimum $(I_{r|\min})$ improvement indices, with respect to the number of passes (N), initial depth $(\mathscr{d}_0)$, and lateral offset distance from the centreline of the lane (LO), are identified along the *length of interest*.

As shown in Fig. 18 at $\mathscr{d}_0 = 0.35$ *m* following 30 passes of the roller, the improvement indices are reasonably consistent underneath the width of the roller. However, the aforementioned improvement indices gradually decline with an increasing *LO*, presenting a reduced effect of the roller as one moves laterally away from its path. This is to be expected. The material directly underneath the roller would be better confined, and subject to the full force of the impact. Whereas the material adjacent is subject to greater degrees of geometric dispersion, material damping and a reduced effective confinement; all of which are mitigating factors to the effectiveness of compaction.

The distribution of the maximum improvement, and thereby the optimal effect of the roller, is presented in Fig. 19, for $N = 5, 10, 30$ passes for $L = 0.25$ and 1 N/node. As can be seen, there is reasonable agreement between $L = 0.25$ and 1 N/node. The differences are attributed to the greater range of motion, and thereby impact forces.

By defining *significant improvement* as being where $I_r > 25\%$, the zone of such significant improvement is estimated to be at 0.8 – 1.2 m depth underneath the width of the roller, after $N = 30$ passes. This agrees well with the depth of major improvement (DMI) estimate, as defined by Scott et al. (2019b), where $DMI = 1.16$ m. By defining *residual improvement* to be estimated for where $25\% \geq I_r \geq 5\%$, this zone is estimated to be 1.25 m laterally and 2.5 m deep, after $N = 30$ passes. Although the maximum depth of the zone of residual improvement is estimated beyond the effective depth of improvement (EDI), as defined by Scott et al. (2019b), where $EDI = 1.74$ *m*, it may still yet be indicative of the zone of influence. Various field investigations (Clifford 1978;

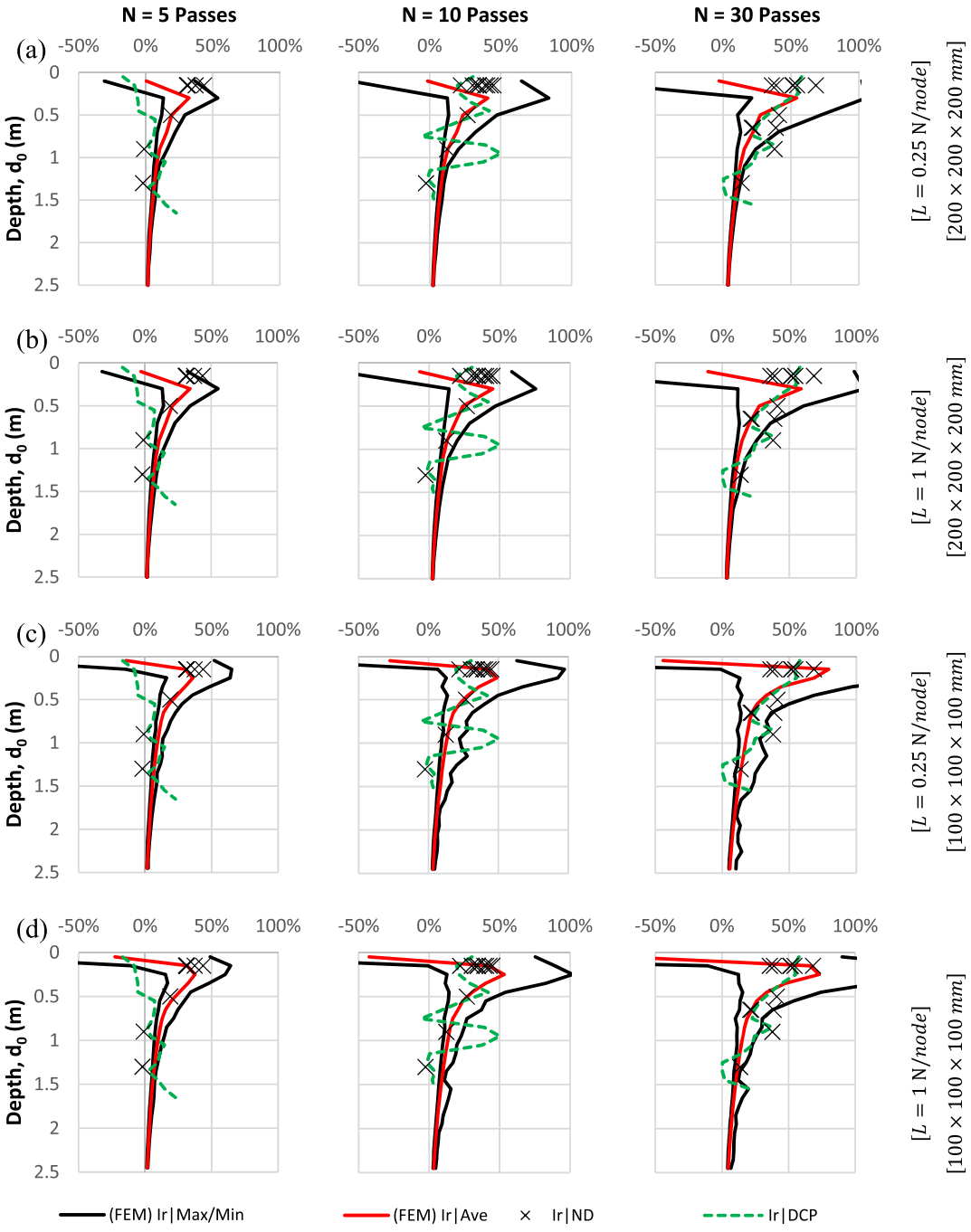

Fig. 20. Improvement index profiles for N = 5, 10, 30 passes: [using 200 × 200 × 200mm FEs] (a) $L = 0.25$ N/node; (b) $L = 1$ N/node; [using 100 × 100 × 100 mm FEs] (c) $L = 0.25$ N/node; and (d) $L = 1$ N/node.

Avalle 2004, 2007; Avalle & Carter, 2005; Avalle & Mackenzie, 2005; Scott & Jaksa 2015) have shown that RDC with a BH–1300 4-sided 8 tonne impact roller influences soils beyond 2 m depth.

As shown in Fig. 20, the numerical model results are benchmarked against the field trial, for each simulation, where the maximum $\left(I^*_{r|\max}\right)$, average $\left(I^*_{r|ave}\right)$, and minimum $\left(I^*_{r|\min}\right)$ improvement indices are identified with respect to $N = 5, 10, 30$ passes and $\mathscr{A}_0$, across the width of the roller, and along the *length of interest* are presented. The results show reasonable agreement with the field trial results presented in Section 3.2.

For the most part, the results between simulations using the fine and coarse FE mesh resolution, $L = 0.25, 1$ N/node, are consistent with the field data. However, the coarse mesh is subject to a larger discretization error, as the forces are transmitted over a larger volume through each element, mitigating the pressure and hence the degree of compaction.

There is a marginal difference between the results for $L = 0.25$, 1 N/node. This difference is likely the result of the roller's motion behaving more erratically for the lower loading, where a more variable motion with an instance of 'skipping motion' is observed, as discussed previously in Section 4.2.1.

5. Conclusions

This paper has presented the results of finite element modelling of rolling dynamic compaction using the Broons BH–1300 4-sided 8–tonne impact roller on a coarse-grained soil subjected to up to 30 passes. The results have shown that the FE model, in conjunction with the methodology described above, can represent the *typical motion* of the roller and provide reasonable estimates for the settlement and improvement profile of the soil. The determination of the input for GCM (i.e. Mat_025) from more commonly understood engineering parameters (Cam Clay and Mohr Coulomb) gives a reasonably good prediction of experimental and field data. This is despite foregoing the kinematic hardening feature of the constitutive material model.

The FE model showed that the near surface soils are highly disturbed to approximately 0.2–0.3 m depth, whilst maximum compaction is typically achieved between 0.3 and 0.5 m depth. Significant improvement ($I_r > 25\%$) of the soil is shown to be directly underneath the width of the roller to approximately 0.8 – 1.2 m depth; in agreement with $DMI = 1.16$ m. A residual improvement ($25\% \geq I_r \geq 5\%$) is shown to extend to approximately to 2.5 m depth, and 1.25 m laterally, which may be representative of the zone of influence.

The simulations suggest densification of the soil is not necessarily consistent along the path of the roller. This is likely due to the formation of the undulating surface profile, which in turn informs the positioning of the roller with each successive pass, becoming regular. For as the positioning of the roller becomes regular, the roller impacts the soil at regular intervals.

There is general agreement between the simulations. As expected, a finer mesh ($100 \times 100 \times 100$ mm) is more accurate, and perhaps a resolution finer still is necessary to better represent the soil; however, at greater computational cost. Nevertheless, the coarse FE mesh ($200 \times 200 \times 200$ mm) can reasonably reproduce field data and is useful in investigating the potential of RDC.

There is potential to improve upon the FE model. A limitation of the present FE model is the absence of adequately accounting for rate-dependent behaviour and vibration induced compaction, which is likely experienced in the field within the zone of influence. Further, the implementation of the roller's motion beyond the prescribed *typical motion* by potentially expanding the FE model to include the double linkage spring mechanism, or an improved understanding of the kinematics of the roller, may improve accuracy. Lastly, during the resetting phase, the soil is subject to disturbance, as the module is released/dropped on to the soil (see Fig. 12). An alternative approach for the implementation of the multiple pass scenario may be necessary for a larger number of passes and highly deformable soils, whereby the disturbance may be more pronounced.

Although the undertaking of FEM and subsequent post-analysis is heavily computer resource and time intensive, the numerical study provides an alternative to investigating the potential of RDC for which is typically undertaken through field trials. The appropriate use of the FEM presented herein may provide greater insights into relationships between the initial conditions (soil parameters, roller design, and roller kinematics) and to the resulting settlement and improvement profiles.

CRediT authorship contribution statement

Andrew C. Bradley: Conceptualization, Methodology, Software, Validation, Formal analysis, Investigation, Writing – original draft, Visualization. **Mark B. Jaksa:** Supervision, Writing – review & editing. **Yien-Lik Kuo:** Writing – review & editing.

Declaration of Competing Interest

The authors declare that they have no known competing financial interests or personal relationships that could have appeared to influence the work reported in this paper.

Data availability

Data will be made available on request.

Acknowledgements

The authors appreciate the assistance of Mr. Gary Bowman, Drs. Brendan Scott and Terry Bennett at the University of Adelaide. The authors are grateful to Mr. Stuart Bowes from Broons who provided the impact roller used in the field study; and Monarto Quarries personnel, who supplied plant and quarry material.

References

Avalle, D.L., 2004. Ground improvement using the "square" impact roller - case studies. Kuala Lumpur, Malaysia, CI-Premier, pp. 101–108.
Avalle, D.L., 2007. Trials and validation of deep compaction using the "square" impact roller. Australia, Australian Geomechanics Society, Sydney, pp. 63–69.
Avalle, D.L., Carter, J.P., 2005. Evaluating the improvement from impact rolling on sand. Coimbra, Portugal, CI-Premier, pp. 153–160.
Avalle, D.L., McKenzie, R.W., 2005. Ground improvement of Landfill site using the "square" impact roller. Aust. Geomech. 40 (4), 15–21.
Bastaee, B., Parvizi, M., 2012. Experimental and numerical analysis of impact roller on clay overlaying sand. SPIE, Yasouj.
Belytschko, T., Bindeman, L.P., 1993. Assumed strain stabilization of the eight node hexahedral element. Comput. Methods Appl. Mech. Eng. 105 (2), 225–226.
Boussinesq, J.V., 1885. Applications des potentiels à l'étude de l'équilibre et du mouvement des solides élastiques. Gauthier-Villars, Paris.
Bowles, J.E., 1997. Foundation analysis and design, fifth ed. McGraw-Hill, Singapore.
Bradley, A.C., Crisp, A.C., Jiang, J.H., Power, C.N., 2012. Assessing the effectiveness of rolling dynamic compaction using LS-DYNA. School of Civil Environmental and Mining Engineering, University of Adelaide, Adelaide, Australia.
Bradley, A.C., Jaksa, M.B., Kuo, Y.L., 2019. Examining the kinematics and energy of the four-sided impact roller. In: Proceedings of the Institution of Civil Engineers - Ground Improvement, 172(4), pp. 297-304.
Bradley, A.C., Jaksa, M.B., Kuo, Y.L., Bennett, T., 2015. A finite element model for heavy tamping on dry sand. Scotland, ICE Publishing, Edinburgh, pp. 1377–1382.
Canala, G.S., Gauro, C.A., March, J.C., Strapps, R.W., 2014. Final Research Project Report: Quantifying the effectiveness of the four-sided impact roller with operating speed. University of Adelaide, Adelaide, Australia.
Chen, Y., Jaksa, M., Kuo, Y., Scott, B., 2021. Discrete Element Modelling of the 4-sided Impact Roller. Computer Geotechnics 137 (104236).
Clifford, J.M., 1975. An introduction to impact rollers. National Institute for Road Research, Internal report RP/2/75, South Africa: s.n.
Clifford, J.M., 1978. Evaluation of compaction plant and methods for the construction of earthworks in Southern Africa, Durban, South Africa: MSE thesis, University of Natal.
Clifford, J.M., Bowes, G., 1995. Calculating the energy delivered by an impact roller. In: A trilogy of Papers for the Sept. 1995 Lecture Tour and International Seminars to commemorate the 10th Anniversary of the BH 1300 Standard Impact Roller, Paper Two, s.l.: s.n.
Ellis, C.I., 1979. Pavement engineering in developing countries. Transport and Road Research Laboratory, TRRL Supplementary Report 537, Crowthorne, Berkshire: s.n.
Gu, Q., Lee, F.H., 2002. Ground response to dynamic compaction of dry sand. Geotechnique 52 (7), 481–493.
Isenberg, J., Vaughan, D.K., Sandler, I., 1978. Nonlinear soil-structure interaction. Weidlinger Associates, s.l.
Kim, K., 2010. Impact rollers (soil compaction) numerical simulation of impact rollers for estimating the influence depth of soil compaction, 1st ed. LAP LAMBERT Academic Publishing GmbH & Co. KG, Saarbrucken.
Knappett, J.A., Craig, R.F., 2012. Craig's Soil Mechanics, 8th ed. Spon Press, New York, United States of America.
Kuo, Y.L. et al., 2013. Assessing the effectiveness of rolling dynamic compaction. In: Paris Proc. of the 18th Int. Conf. on Soil Mechanics and Geotechnical Engineering, pp. 1309-1312.
Liu, J.H., 2013. A study of the mechanical behaviour of cemented soils via structured cam clay. University of Wollongong, Wollongong, NSW, Australia.
Liu, M.D., Carter, J.P., 2002. Structured cam clay model. Can. Geotech. J. 39 (6), 1313–1332.
Li, Y., 2021. Evaluating the Effectiveness of Rolling Dynamic Compaction via Scaled Model and Numerical Simulation. University of Sydney, Sydney.
Lstc, 2015. LS-DYNA KEYWORD USER'S MANUAL. Livermore Software Technology Corporation, Livermore, California.
Santamarina, J.C., Park, J., 2016. Geophysical Properties of Soils. Aust. Geomech. 51 (4), 183–194.
Scott, B.T., Jaksa, M.B., 2014. Evaluating rolling dynamic compaction of fill using CPT. Las Vegas, USA, s.n., pp. 941–948
Scott, B.T., Jaksa, M.B., 2015. The effectiveness of rolling dynamic compaction - a field based study. In: Ground Improvement Case Histories: Compaction, Grouting, and Geosynthetics. Elsevier, Kidlington, Oxford, pp. 429–452.
Scott, B.T., Jaksa, M.B., Mitchell, P., 2019a. Ground response to rolling dynamic compaction. Géotechnique Lett. 9 (2), 99–105.

Scott, B.T., Jaksa, M.B., Mitchell, P., 2019b. Depth of influence of rolling dynamic compaction. In: Proceedings of the Institution of Civil Engineers - Ground Improvement.

Scott, B.T., Jaksa, M.B., Mitchell, P., 2020. Influence of towing speed on effectiveness of rolling dynamic compaction. J. Rock Mech. Geotech. Eng. 12 (1), 126–134.

Scott, B.T., Jaksa, M.B., Syamsuddin, E., 2016. Verification of an impact rolling compaction trial using various in situ testing methods. Gold Coast, Australia, s.n., pp. 735–740

Simo, J.C., Ju, J., Pister, K.S., Taylor, R.L., 1988. Assessment of cap model: consistent return algorithms and rate-dependent extension. J. Eng. Mech. 114 (2), 191–218.

Standards Australia, 1997. AS 1289.6.3.2: Methods of testing soils for engineering purposes Soil strength and consolidation tests - Determination of the penetration resistance of a soil - 9 kg dynamic cone penetrometer test, s.l.: Standards Australia.

Standards Australia, 1998. AS 1289.5.5.1: Methods of testing soils for engineering purposes Soil compaction and density tests - Determination of the minimum and maximum dry density of a cohesionless material - Standard method (Reconfirmed 2016), s.l.: Standards Australia.

Standards Australia, 2006. AS 1289.3.5.1: Methods of testing soils for engineering purposes Soil classification tests - Determination of the soil particle density of a soil - Standard method, s.l.: Standards Australia.

Standards Australia, 2007. AS 1289.5.8.1: Methods of testing soils for engineering purposes Soil compaction and density tests - Determination of field density and field moisture content of a soil using a nuclear surface moisture-Density gauge - Direct transmission mode, s.l.: Standards Australia.

Standards Australia, 2009. AS 1289.3.6.1: Methods of testing soils for engineering purposes Soil classification tests - Determination of the particle size distribution of a soil - Standard method of analysis by sieving, s.l.: Standards Australia.

Standards Australia, 2016. AS 1289.6.4.2: Methods of testing soils for engineering purposes Soil strength and consolidation tests - Determination of compressive strength of a soil - Compressive strength of a saturated specimen tested in undrained triaxial compression with measureme, s.l.: Standards Australia.

Standards Australia, 2017. AS 1289.5.2.1: Methods of testing soils for engineering purposes Soil compaction and density tests - Determination of the dry density/moisture content relation of a soil using modified compactive effort, s.l.: Standards Australia.

Standards Australia, 2020. AS1289.6.6.1: Methods of testing soils for engineering purposes Soil strength and consolidation tests - Determination of the one-dimensional consolidation properties of a soil - Standard method, s.l.: Standards Australia.

University of Adelaide, 2020. Phoenix HPC. [Online] Available at: https://www.adelaide.edu.au/technology/research/high-performance-computing/phoenix-hpc.